Scale-dependent air-sea exchange in the polar oceans: floe-floe and floe-flow coupling in the generation of ice-ocean boundary layer turbulence

Samuel Brenner[1], Christopher Horvat[1,2], Paul Hall[1], Anna Lo Piccolo[1], Baylor Fox-Kemper[1], Stéphane Labbé[3], Véronique Dansereau[4]

[1]Brown University, Providence, US
[2]The University of Auckland, Auckland, NZ
[3]Sorbonne Université, Paris, FR
[4]Institut des Sciences de la Terre, Université Grenoble Alpes, CNRS (UMR5275), Gières, FR

Key Points:

- Discrete element model results show floe-size-dependent ice-ocean boundary layer (IOBL) stress-driven turbulence.
- IOBL turbulence is driven both by floe collisional velocity and by floe-scale ocean variability.
- We present a framework for a scale-aware parameterization of IOBL turbulence using bulk parameters.

Corresponding author: Samuel Brenner, sdbrenner@brown.edu

Abstract

Sea ice is a heterogeneous, evolving mosaic comprised of many individual floes, which vary in spatial scales from meters to tens of kilometers. Both the internal dynamics of the floe mosaic (floe-floe interactions), and the evolution of floes under ocean and atmospheric forcing (floe-flow interactions), determine the exchange of heat, momentum, and tracers between the lower atmosphere and upper polar oceans. Climate models do not represent either of these highly variable interactions. We use a novel, high-resolution, discrete element modelling framework to examine the production of ice-ocean boundary layer (IOBL) turbulence within a domain approximately the size of a climate model grid. We show floe-scale effects cause a marked increase in IOBL turbulent production relative to continuum model approaches, and provide a method of representing that turbulence using bulk parameters related to the spatial variance of the ice and ocean: the floe size distribution and the ocean kinetic energy spectrum.

Plain Language Summary

Sea ice is a complex broken mosaic of individual pieces, called floes. These floes control how heat and momentum move between the atmosphere and ocean. But these floes interact with each other as well as with the upper ocean and lower atmosphere, and this means that these exchanges can be complexly related to both types of processes: floe-floe and floe-flow. Using experiments that explicitly evolve sea ice floes interacting with each other and the upper ocean, we develop a formulation for how momentum is transferred between the ice and ocean as a function of simple parameters of the ice-ocean system that may be available to climate models.

1 Introduction

A key component of Earth's climate system, sea ice is a primary mediator of exchange across the atmosphere-ocean boundary in polar regions. Ongoing Arctic sea ice loss (e.g., Meier & Stroeve, 2022, and others) and changes in Antarctic sea ice (e.g., Eayrs et al., 2021) therefore will lead to changes in air-sea coupling. The shift to a more seasonal Arctic sea ice regime and relative expansion of marginal ice zones (MIZs; Strong & Rigor, 2013; Rolph et al., 2020) may lead to increased ocean mixing (Rainville et al., 2011) due to the declining role of ice internal stress, which disrupts wind-momentum transfer (e.g., Martin et al., 2014; Brenner et al., 2021, 2023). That shift might modify Ekman pumping, ocean overturning, and freshwater storage in the Arctic Ocean (Wang et al., 2019; Wu et al., 2021). It also would alter sub-ice-surface oceanic eddy fields (Armitage et al., 2020) and mixed layer depths, which are regulated in part by frictional effects in the ice-ocean boundary layer (Ou & Gordon, 1986; Meneghello et al., 2020; Manucharyan & Thompson, 2022).

Sea ice is a composite of pieces, called floes, that vary in size over scales from meters to tens of kilometers across (e.g., Stern et al., 2018; Horvat et al., 2019). Yet when considering air-sea coupling at climate model scales, the role of sea ice variability is typically collapsed to a single metric: the sea ice concentration (SIC), c. In models, the net ocean/atmosphere surface fluxes in a model grid cell are typically calculated through "flux-averaging" (e.g., Claussen, 1990). For some field, χ (e.g., heat, momentum), the net surface flux, F_χ is:

$$(F_\chi)_{\text{net}} = c(F_\chi)_{io/ia} + (1-c)(F_\chi)_{ao}, \tag{1}$$

the ice concentration-weighted sum of the atmosphere-ocean (subscript ao) and ice-ocean/ice-atmosphere fluxes (subscript io/ia). However, when the floes are resolved, the concentration fields and concentration-weighted fluxes are a suitable measure only of the averaged conditions, not the pointwise conditions which vary intermittently due to the presence or absence of a floe.

It is well-known that a variety of exchange processes are heavily affected by floe-scale variability. *Floe-floe* interactions determine the evolution of sea ice through granular rheological laws for ice internal stresses within the MIZ (Shen et al., 1987; Feltham, 2008; Herman, 2013), which remain an active area of research (e.g., Rynders et al., 2022; Herman, 2022) that is not implemented in current-generation climate models. Coupled interactions between floes and the ocean and atmosphere (*floe-flow* interactions) impact both atmospheric boundary layer and ice-ocean boundary layer (IOBL) processes (e.g., Horvat et al., 2016; Gupta & Thompson, 2022; Wenta & Herman, 2018, 2019). Additionally, ice-ocean and ice-atmosphere drag is highly dependent on sea ice geometry, but existing approaches for bulk formulations of air-sea momentum exchange (Lüpkes et al., 2012; Tsamados et al., 2014) fail to account for a variable distribution of floe sizes (Brenner et al., 2021; Bateson, 2021).

In this work, we explore the dual roles of floe-floe and floe-flow dynamics on ice-ocean exchange using a novel discrete element model of sea ice floe dynamics (Rabatel, 2015; Rabatel et al., 2015), forced by variable ocean currents that are derived from simulations of an ice edge with only air-sea heat fluxes and brine rejection, not wind stresses (Lo Piccolo, 2021; Lo Piccolo et al., 2023).

2 Background and Methods

2.1 Parameterization of ice-ocean turbulent exchange

Bulk drag laws parameterize local turbulent ocean-ice momentum flux, $\boldsymbol{\tau}_{oi}$, across the IOBL in terms of differences between sea ice velocity $\boldsymbol{u}_i$, and near-surface ocean ve-

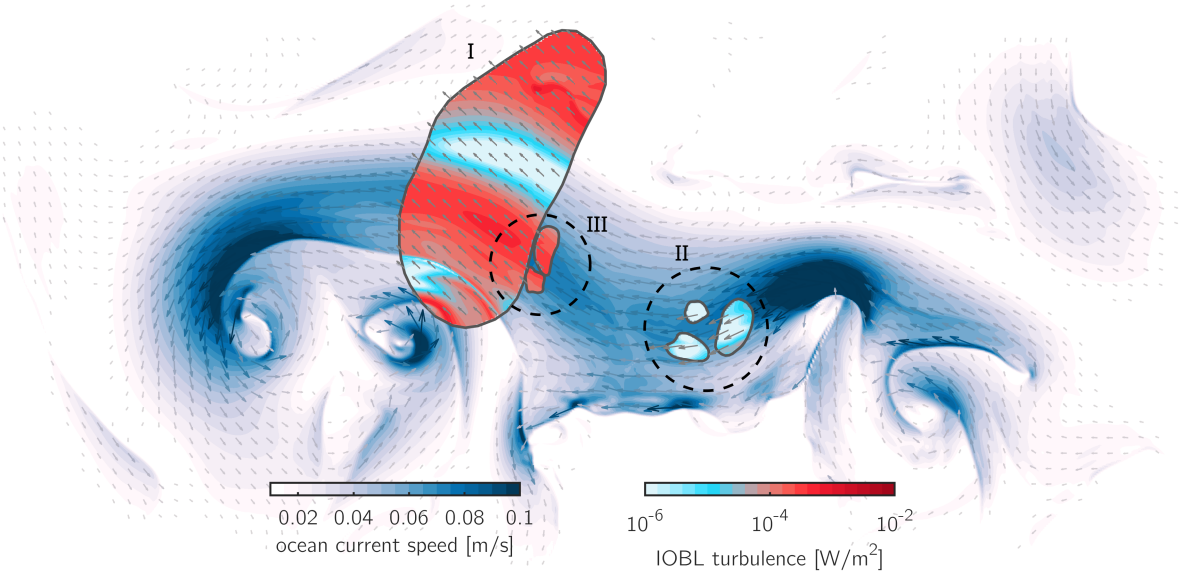

Figure 1: A schematic showing how scale mismatches between ocean flow (blue colourmap and background vectors) and ice velocity (vector arrows over ice floes) contribute to IOBL shear production, $\mathcal{S}$ (cyan/red colourmap).

locity $\boldsymbol{u}_o$, via the ice-ocean relative velocity, $\boldsymbol{u}_{rel} = \boldsymbol{u}_o - \boldsymbol{u}_i$:

$$\boldsymbol{\tau}_{oi} = \rho_o C_{io}(\boldsymbol{u}_{rel})\|\boldsymbol{u}_{rel}\|, \tag{2}$$

where ρ_o is the ocean density and C_{io} is a turbulent transfer coefficient (McPhee, 1980). The importance of relative velocities in air-sea fluxes has been recently emphasized in damping submesoscales (Renault et al., 2016; Delpech et al., 2023), and the interest here is in examining ice-ocean stresses. Boundary stresses drive the production, $\mathcal{P}$, of turbulent kinetic energy (TKE) via shear,

$$\mathcal{P} = \boldsymbol{\tau} \cdot \frac{\partial \boldsymbol{u}}{\partial \boldsymbol{x}} \tag{3}$$

Vertically integrating over the IOBL yields a total turbulent production of TKE:

$$\mathcal{S} \equiv \int \mathcal{P}\, \mathrm{d}z \sim \boldsymbol{\tau}_{oi} \cdot \boldsymbol{u}_{rel} = \rho_o C_{io}\|\boldsymbol{u}_{rel}\|^3. \tag{4}$$

This production is then dissipated by small-scale turbulent motions (e.g. Smith & Thomson, 2019), including mixing and creating potential energy, with consequences for air-sea and ice-ocean transfers and oceanic boundary layer energy and depth. Thus the effect of ice-ocean velocity differences is to produce turbulent kinetic energy at a rate ε from the shears and stresses related to larger-scale ocean flows and ice floe motions, where $\int \varepsilon\, \mathrm{d}z \sim \mathcal{S}$, damping variability in the ocean current field (e,g., Shrestha & Manucharyan, 2021; Manucharyan & Thompson, 2022; Brenner et al., 2023).

Representation of sea ice as solid-body floes—as opposed to traditional continuum models (e.g., Golden et al., 2020)—introduces constraints on the ice velocity field, leading to production/dissipation of TKE that is highly dependent on the relative spatial scales of ice floes to ocean flow. Large floes compared to the scale of ocean variability generate more turbulence than small floes (c.f., floes I and II in Figure 1) due to ice-ocean

velocity mismatches over the size of the floe. Furthermore, collisions can limit correlated ice-ocean motion (floes III in Figure 1). In the work to follow, we will focus on understanding and parameterizing $\mathcal{S}$.

2.2 Sea ice discrete element model

We use a discrete element model known as "FloeDyn", which describes the dynamics of assemblies of individual sea ice floes (Rabatel, 2015; Rabatel et al., 2015). The floes act as rigid bodies that move in response to atmospheric or oceanic forcing and due to floe collisions. Between collisions, the translational and angular velocities, $\boldsymbol{U}_i$ and ω_i, respectively, for each ice floe are given by:

$$M\frac{\mathrm{d}\boldsymbol{U}_i}{\mathrm{d}t} = M\boldsymbol{\mathcal{F}} + \int_A (\boldsymbol{\tau}_{ai} + \boldsymbol{\tau}_{oi})\,\mathrm{d}A, \tag{5a}$$

$$I\frac{\mathrm{d}\omega_i}{\mathrm{d}t} = \int_A (\boldsymbol{x} - \boldsymbol{x}_c) \times (\boldsymbol{\tau}_{ai} + \boldsymbol{\tau}_{oi})\,\mathrm{d}A, \tag{5b}$$

where M is the mass of the floe, $\boldsymbol{\tau}_{ai}$ and $\boldsymbol{\tau}_{oi}$ are, respectively, the atmosphere-ice and ocean-ice stresses (in our simulations there are no wind stresses applied to either ice or ocean, so $\boldsymbol{\tau}_{ai} = 0$), $\boldsymbol{\mathcal{F}}$ represents other external body forces, I is the moment of inertia, and $\boldsymbol{x}$ is the position vector with $\boldsymbol{x}_c$ the position of the floe centroid. Ice interactions are modelled as a linear complimentary problem using Coulomb's law (see Rabatel et al., 2015, for further details).

While Rabatel et al. (2015) only include the body force associated with the Coriolis effect, we implemented an additional gravitational body force due to the mean sea surface tilt over a floe and the total body force applied in Equation (5a) is the combination of these two.

Because floes move with the area-integrated stress, the leading-order steady-state solution to Equation (5a) (found by linearizing $\boldsymbol{\tau}_{oi}$ about small relative velocity) gives the floe translation velocity as matching the mean ocean velocity under it: $\boldsymbol{U}_i \sim \langle \boldsymbol{u}_o \rangle$ (where $\langle\cdot\rangle$ denotes the areal mean over a floe). Similarly, the angular velocity of a floe in steady-state matches the ocean vorticity field: $\omega_i \sim \frac{1}{2}\langle \zeta_o \rangle$ (where the factor of $1/2$ arises due to the relationship between angular velocity and vorticity), a fact that has been exploited in remote-sensing reconstructions of upper-ocean vorticity (Lopez-Acosta et al., 2019, Manucharyan, Lopez-Acosta, & Wilhelmus, 2022).

2.3 Model configuration and experiments

We run a series of one-way forced FloeDyn experiments using ocean surface currents (top 2.5m) provided by a separate ocean simulation. This ocean simulation (from Lo Piccolo, 2021; Lo Piccolo et al., 2023) uses the Massachusetts Institute of Technology general circulation model (MITgcm; Marshall et al., 1997) to investigate submesoscale energy transfers at a sea ice edge. It considers an ocean domain half-covered by sea ice and forced by a cold atmosphere, leading to rapid refreezing and brine rejection in the ice-free part of the domain. The resulting spatial gradient in buoyancy flux leads to an active eddy field (Figures 3a and 3b) as available potential energy (APE) is converted to eddy kinetic energy (EKE). We forced the FloeDyn with currents from a 5-day subset at the end of the ocean simulation (days 25–30) when eddies have saturated the domain, but include no thermodynamic effects or feedbacks to the ocean model.

Each FloeDyn simulation has the ocean surface randomly populated by sea ice floes of varying sizes and shapes. Here, floe size refers to the effective floe radius, r, defined in terms of floe surface area: $r = \sqrt{A/\pi}$. Floe sizes were selected following truncated power-law FSDs (e.g., Stern et al., 2018) with number density $N(r) = Cr^{-\alpha}$ in the interval $r \in [r_{\min}, r_{\max}]$, where $N(r)\,\mathrm{d}r$ describes the number of floes per unit area with size between r and $r + \mathrm{d}r$, and $\int_{r_{\min}}^{r_{\max}} (\pi r^2) N(r)\,\mathrm{d}r = c$ (the SIC). For truncated distri-

butions, the complementary cumulative distribution function is concave-down (Stern et al., 2018). We performed simulations over a range of SICs for three different FSDs. Each FSD had the same power-law exponent, $\alpha = 2$, and same minimum floe size, with varying maximum floe sizes (Figure 3c), defining "large", "medium", and "small" FSD cases. Floe shapes were selected from a library of shapes extracted from sea ice imagery (Rabatel et al., 2015), which include non-convex outlines. For floes within this library, mean caliper diameters ranged from $\sim 2r$ to $\sim 2.3r$. For each FSD, we tested fractional SICs in 0.1 increments from 0.1 to 0.8 (large FSD), 0.7 (medium), and 0.6 (small). The maximum SIC we examine is smaller for smaller floes due to geometrical and numerical constraints.

Ocean surface currents were supplied to FloeDyn within a 50 km×50 km periodic domain at a 50 m horizontal grid resolution and 4 h temporal resolution. Currents were linearly interpolated (in space and time) to the locations of sea ice mesh points at each calculation timestep. FloeDyn uses an adaptive timestepping mechanism to avoid floe interpenetration so calculation timesteps varied throughout each simulation, but a default timestep of 30 s is used in the absence of collisions. Model snapshot output is at each 1 h, and sub-sampled to match the 4 h ocean forcing. The first 8 h of each simulation were discarded as a spin-up time as floes started from rest (similar to Manucharyan, Lopez-Acosta, & Wilhelmus, 2022). Floe translational and rotational velocity outputs ($\boldsymbol{U}_i$ and ω_i) and binary masks of the floe positions were then used to reconstruct the full ice velocity field on the input forcing grid at each timestep and an estimate of IOBL-integrated TKE production, $\mathcal{S}$, was calculated following Equation (4). The process results in some discretization errors for the smallest ice floes, but we find this does not materially affect the results we present below.

2.4 Velocity decomposition

To analyse aggregate results and understand grid-scale IOBL TKE production, we perform a floe-by-floe Reynolds-type decomposition of the ice-ocean relative velocity. Over each sea ice floe, ice and ocean velocity fields are separated into means and perturbations: $\boldsymbol{u} = \langle \boldsymbol{u} \rangle + \boldsymbol{u}'$. The spatially-varying ice velocity field, $\boldsymbol{u}_i(\boldsymbol{x})$, is a combination of the translational and angular motions of the floe: $\langle \boldsymbol{u}_i \rangle = \boldsymbol{U}_i$, and $\boldsymbol{u}_i' = \omega_i \hat{k} \times (\boldsymbol{x} - \boldsymbol{x}_c)$. The ice-ocean relative velocity for each floe can be written as:

$$\begin{aligned} \boldsymbol{u}_{rel} &= [\langle \boldsymbol{u}_o \rangle - \langle \boldsymbol{u}_i \rangle] + \boldsymbol{u}_o' - \boldsymbol{u}_i' \\ &= [\langle \boldsymbol{u}_o \rangle - \boldsymbol{U}_i] + \boldsymbol{u}_o' - \omega_i \hat{k} \times (\boldsymbol{x} - \boldsymbol{x}_c)\,. \\ &\equiv \boldsymbol{\delta}_{oi} + \boldsymbol{u}_o' - \boldsymbol{u}_i'. \end{aligned} \tag{6}$$

Since we expect $\boldsymbol{U}_i \sim \langle \boldsymbol{u}_o \rangle$ for non-interacting floes (Section 2.2), the term $\boldsymbol{\delta}_{oi}$ reflects the velocity differences arising from floe-floe interactions.

When computing the local turbulence production, we note that Equation (4) depends on the relative velocity *magnitude*. Then taking the floe-average of the inner product of Equation (6) with itself, we find:

$$\left\langle \|\boldsymbol{u}_{rel}\|^2 \right\rangle \overset{\boldsymbol{u}_i' \ll (\boldsymbol{\delta}_{oi} + \boldsymbol{u}_o')}{\sim} \left\langle \|\boldsymbol{\delta}_{oi} + \boldsymbol{u}_o'\|^2 \right\rangle, \tag{7}$$

where we have neglected the (small, see below) rotational term. Defining $\overline{\cdot}$ as an average over many floes of the same size, we further approximate:

$$\overline{\left\langle \|\boldsymbol{u}_{rel}\|^2 \right\rangle} \overset{\overline{\langle \boldsymbol{\delta}_{oi} \cdot \boldsymbol{u}_o' \rangle} \sim 0}{\sim} \overline{\left\langle \|\boldsymbol{\delta}_{oi}\|^2 \right\rangle} + \overline{\left\langle \|\boldsymbol{u}_o'\|^2 \right\rangle} \tag{8a}$$

and

$$\overline{\left\langle \|\boldsymbol{u}_{rel}\|^3 \right\rangle} \sim \overline{\left\langle \|\boldsymbol{\delta}_{oi}\|^3 \right\rangle} + \overline{\left\langle \|\boldsymbol{u}_o'\|^3 \right\rangle} \tag{8b}$$

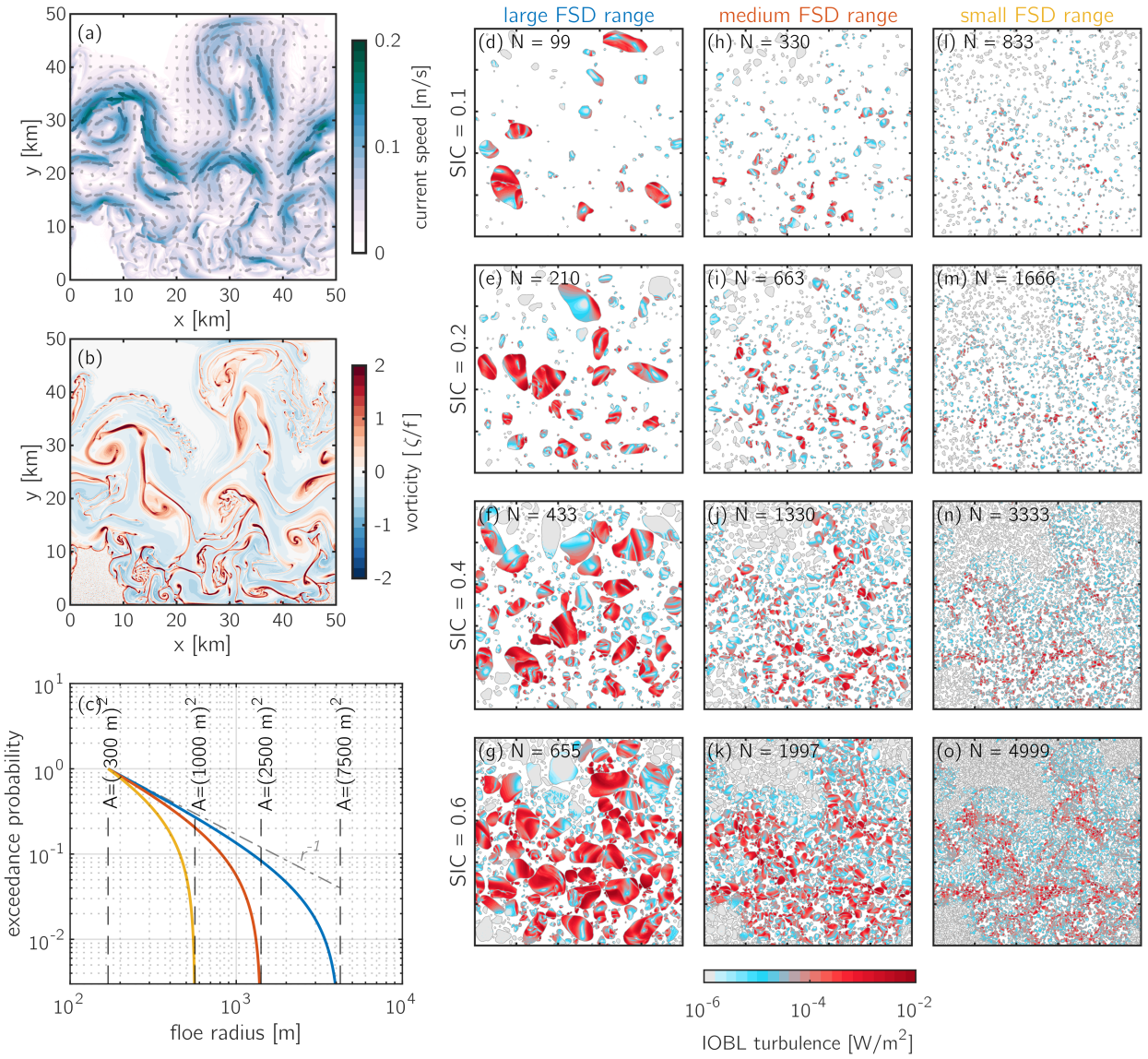

Figure 2: Snapshots of the ocean surface current velocity field (a) and associated vorticity (b) used to force the sea ice model. (c) Complementary cumulative distributions of number of floe sizes for the three different FSD cases tested. (d-o) Snapshots of sea ice floe configurations for the different FSD cases (columns) for example SICs (rows) and associated fields of IOBL turbulence, $\mathcal{S}$. Labels on each of the panels show the number of ice floes, N, for a given simulation.

where we then assume that $\boldsymbol{\delta}_{oi}$ and $\boldsymbol{u}'_o$ are uncorrelated over many random floe configurations. Thus Equation (8) partitions the average relative velocity magnitude into separate contributions from *floe-floe interactions* and *floe-flow interactions*. As shown in (4), the relative velocity magnitude is the key agent for production of IOBL turbulence.

3 Results

3.1 Coupling between ice floe velocities and ocean currents

The leading order solutions of Equation (5) suggest that non-interacting floes move with the floe-mean ocean current field: $\boldsymbol{U}_i \sim \langle \boldsymbol{u}_o \rangle$ and $\omega_i \sim \frac{1}{2}\langle \zeta_o \rangle$ (Section 2.2). In low SIC simulations, floe velocities generally matched these solutions (Figures 5a and 5b). Deviations from the expected leading-order solutions were primarily observed for floes impacted by collisions (using cumulative impulse magnitude received by a floe as a measure of the intensity of collisions, with redder colours indicating more intense collisions).

As SIC increases, an increase in collisions causes greater decoupling between sea ice and ocean velocities (Figures 5c to 5f). Yet at all SICs, a subset of floes have ice velocities highly correlated with floe-averaged ocean velocities (tan-coloured points concentrated on the 1:1 or 1:2 lines in Figures 5a to 5f). This confirms the interpretation of $\boldsymbol{\delta}_{oi}$ as representative of ice dynamic forces (Section 2.4).

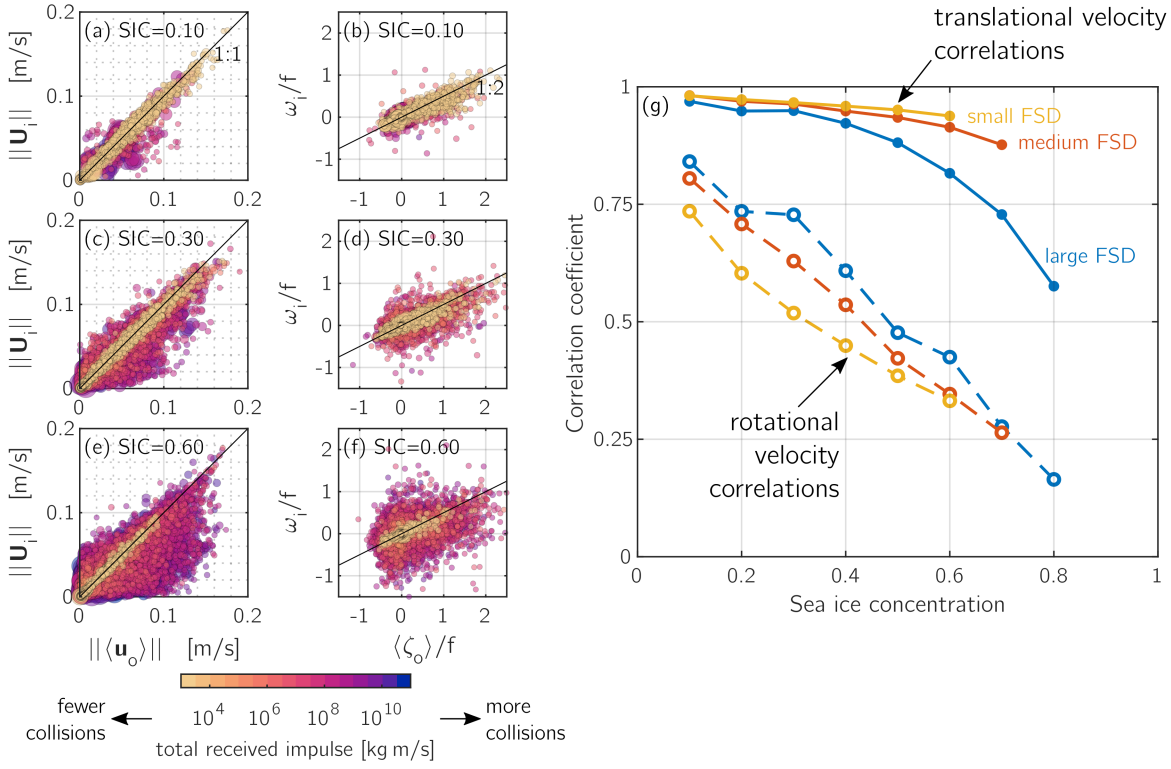

Figure 4: (a) Scatter plots comparing sea ice translational velocity (y axis) to floe-averaged ocean velocity (x-axis) for a low SIC simulation. (b) Same, for rotational velocities. (c,d; e,f) Same as (a,b) but for 30% SIC or 60% SIC. Colours are integrated received impulse, a measure of total collisional energy imparted to each floe. (g) Floe ensemble-average correlation of (solid) translational motions and (dashed) rotational motions as a function of SIC and FSD.

Correlation coefficients over all floes in each simulation between $\langle \boldsymbol{u}_o \rangle$ and $\boldsymbol{U}_i$ (taken as the magnitude of the vector correlation; solid lines in Figure 5g) and between $\langle \zeta_o \rangle$ and ω_i (dashed lines) provide bulk measures of ice-ocean dynamic coupling. At low SICs, $\langle \boldsymbol{u}_o \rangle$ and $\boldsymbol{U}_i$ are highly correlated for all FSDs (e.g., correlation coefficients of $\sim$ 0.98 for SIC = 0.1). As SIC increases, the correlations diverge for the different FSD cases, with a greater decline for the large FSD range compared to the small and medium cases. Correlations for rotational motion ($\langle \zeta_o \rangle, \omega_i$) are lower than for translational motions, even at low SIC, and degrade more rapidly with increasing SIC. These simulations highlight meaningful sea ice dynamic interaction forces for SIC below 0.80 that are highly dependent on both SIC and the FSD.

3.2 IOBL turbulence

IOBL TKE production, $\mathcal{S}$, varies across simulations, as illustrated in Figures 3d to 3o and Figure 7a. The domain average TKE production $\widetilde{\mathcal{S}}$ (where $\widetilde{\cdot}$ denotes a domain-mean) exponentially increases with SIC for all three FSDs (Figure 7a solid lines). This highlights the importance of dynamic processes in modifying ice-ocean coupling, as $\widetilde{\mathcal{S}}$ would otherwise be expected to scale linearly with SIC according to the flux-averaging approach from (1), or even potentially expected to be zero for all concentrations based on no wind stress to drive the ice and ocean differently.

Scale-dependent effects schematized in Figure 1 are evident in simulations at low SIC (e.g., Figures 3d, 3h and 3l). There is noticeably more TKE production for the largest floes in Figure 3d (large FSD), and a drop-off for smaller floe sizes. As SIC increases, the floe-size-dependence partly breaks down: in Figure 3g, there is high turbulence associated with many of the smaller floes as they interact with or become trapped by larger floes (similar to III in Figure 1). While that still occurs for the other FSDs (e.g., Figures 3k and 3o), the smaller range of sizes in those cases allows for floes to more easily move together or move past each other. High turbulence production in the small FSD case is largely confined to zones of oceanic convergence (Figure 3o), which in turn is a characteristic of the submesoscale flow (D'Asaro et al., 2018). As seen in Figures 3d to 3o, the scale-dependence of $\mathcal{S}$ is a statistical effect—the TKE production over any individual floe is heavily influenced by its location relative to the energetic ocean currents.

We examine the dual contributions of ocean variability and sea ice dynamics to $\widetilde{\mathcal{S}}$ by calculating turbulent production using, respectively, $\rho_o C_{io} \|\boldsymbol{u}_o'\|^3$ and $\rho_o C_{io} \|\boldsymbol{\delta}_{io}\|^3$ in place of Equation (4) (Figures 7b and 7c). The relatively small residual between the combined contributions and the total (compare solid curve to black lines) confirms that the rotation term in Equation (6) is of secondary importance as assumed in Equation (8). For low SIC, ice dynamics had a minimal impact on the IOBL turbulence for all FSDs, consistent with the low occurrence of collisions (Section 3.1, Figures 5a and 5b). In these low SIC ranges, $\widetilde{\mathcal{S}}$ primarily results from ocean dynamics contributions. As those contributions depend strongly on the floe scale (Figure 1), the separation of $\widetilde{\mathcal{S}}$ for different FSD cases in Figure 7a can be attributed almost entirely to $\boldsymbol{u}_o'$. Increasing SIC is accompanied by an an exponential increase in the turbulence associated with ice dynamics for all FSDs, while ocean dynamics effects only scale linearly with SIC.

3.3 A framework for parameterizing IOBL turbulence production

A scaling framework for the total IOBL TKE production follows from Equation (4) with the decomposition in Equation (8a). Together, we use them to give an approximate expression for the ensemble-average estimated TKE production for each floe (indexed by n). Then $\langle \mathcal{S} \rangle_n$ is,

$$\langle \mathcal{S} \rangle_n \sim \rho_o C_{io} \left[\left\langle \|\boldsymbol{u}_o'\|^2 \right\rangle_n + \left\langle \|\boldsymbol{\delta_{io}}\|^2 \right\rangle_n \right]^{3/2}, \tag{9a}$$

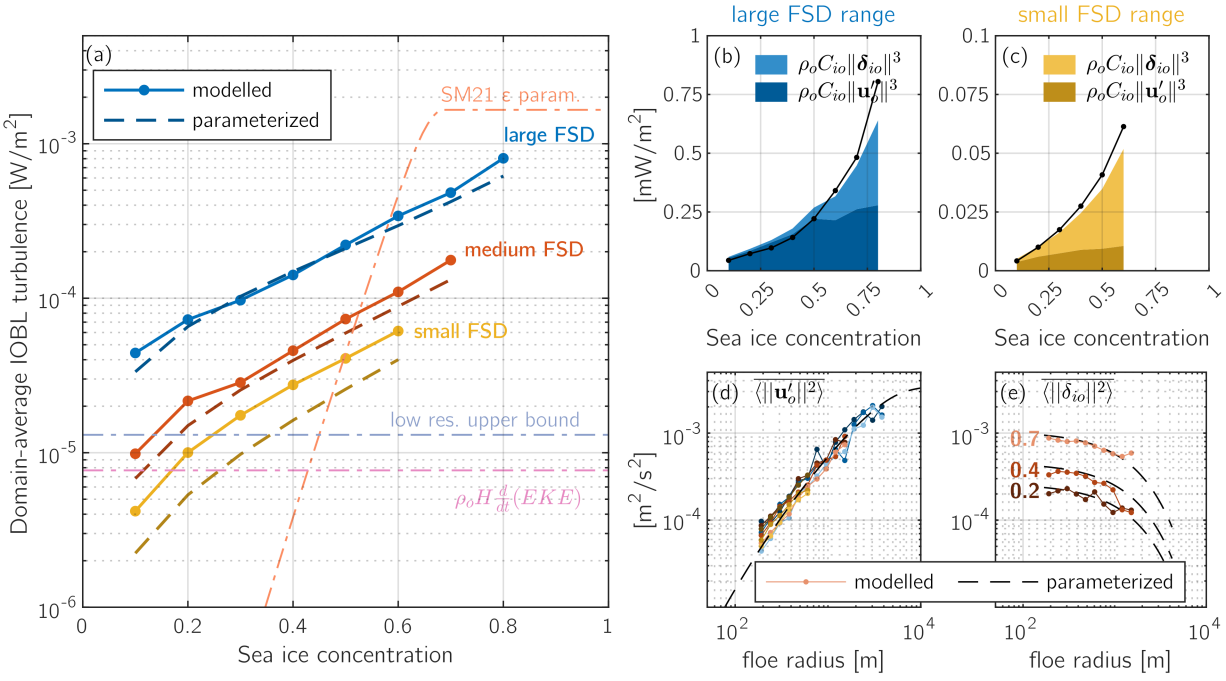

Figure 6: (a) Domain-averaged turbulent production, $\widetilde{\mathcal{S}}$, for the different FSD ranges (as labelled), along with dashed-dot lines relating to contextual values discussed in the text. (b,c) Stacked-area plots showing the relative contributions of ocean dynamics and ice dynamics to $\widetilde{\mathcal{S}}$ for the large/small FSD cases, with black curves showing the total from panel a. (d,e) Bin-averaged and parameterized values of (d) the floe-size-dependent ocean variance (points coloured by FSD range as in panel a, and shaded from dark to light for different SIC cases), and (e) examples from the medium FSD case of the floe-size and SIC dependent $\overline{\langle \|\boldsymbol{\delta}_{oi}\|^2 \rangle}$ (fractional SICs labeled).

where we make the approximation $\langle \|\boldsymbol{u}_{rel}\|^3 \rangle \sim \langle \|\boldsymbol{u}_{rel}\|^2 \rangle^{3/2}$. For the present simulations, this approximation underestimates $\langle \|\boldsymbol{u}_{rel}\|^3 \rangle$ by ~3–10%, but the error introduced will depend on statistical properties of $\|\boldsymbol{u}_{rel}\|$ and may be more significant in other scenarios. Integrating over the entire domain, we then have:

$$\mathcal{S}_{\text{total}} \equiv \sum_n \left(A_n \langle \mathcal{S} \rangle_n \right) \equiv \mathcal{A} \int_0^\infty \pi r^2 N(r) \overline{\langle \mathcal{S} \rangle}(r) \, \mathrm{d}r, \tag{9b}$$

where $A_n = \pi r_n^2$ is the floe area, and $\mathcal{A}$ is the domain area. Because in Section 2 we constructed $\mathcal{S}$ as an ensemble value over all floes of the same area/size, we then are free to recast Equation (9b) in terms of the floe size distribution $N(r)$ (Section 2.3). Our next goal is to approximate the terms that make up Eq. 9a.

3.3.1 Scaling ocean variability

From the relative velocity decomposition (eq. 8a), we see that $\langle \|\boldsymbol{u}_o'\|^2 \rangle$, is the variance of the ocean current field over an individual sea ice floe. Again taking the ensemble average of all floes of size r, we may relate this floe-scale variance to the ocean kinetic energy spectral density. The one-dimensional spectrum, $E(k)$ describes the variance in ocean currents for each wavenumber, k. Thus, a parameterization for $\overline{\langle \|\boldsymbol{u}_o'\|^2 \rangle}$ for a given floe size, r, is based on an appropriate high-pass-filtered spectrum:

$$\mathbb{P}_o(r) \equiv \overline{\langle \|\boldsymbol{u}_o'\|^2 \rangle} = \int_0^\infty \left[1 - \mathrm{sinc}^2 (rk) \right] E(k) \, \mathrm{d}k, \tag{10}$$

where the shape of the high-pass filter reflects that floes are spatial "boxcar" filters of the ocean velocity variance.

Over the full range of simulations, we show in Figure 7d that $\overline{\langle \|\boldsymbol{u}_o'\|^2 \rangle}$, integrated over the FSD, is well predicted by the parameterization $\mathbb{P}_o(r)$ when using the calculated ocean current spectrum. Due to convergence in the ocean currents, floes are not evenly distributed in space, and instead preferentially sample more energetic regions; however, this effect is negligibly small but depends on the Rossby number of the flow (D'Asaro et al., 2018).

Here, by resolving the ocean currents, we can explicitly calculate Equation (10). However in an ocean model, it will be necessary to use existing understanding of the sub-ice ocean variance spectrum (e.g., Timmermans et al., 2012; Timmermans & Marshall, 2020) or more generally for ocean turbulence (e.g., Fox-Kemper et al., 2011). We note that, as in 2D quasigeostrophic turbulence, there is a separation of inertial ranges that can occur below and above the ocean deformation radius, as well as a potential regime shift in sea ice floe variability (e.g., as seen in Gupta & Thompson, 2022).

3.3.2 Scaling ice dynamics

The remaining part of $\mathcal{S}$ is $\boldsymbol{\delta}_{oi}$. This relates to the internal stress dynamics of the sea ice pack, and the correlation of local floe motions with the ocean flow. Within the SIC ranges considered here (≤ 0.8), ice is often considered to be in "free drift", and internal stress dynamics are thought to be negligible. However, as seen in section 3.1, $\boldsymbol{\delta}_{oi}$ is non-zero across the simulations, highlighting that mechanical aspects of sea ice can be important even below SIC ~ 0.8. The theory of how to relate floe-scale mean velocities and ocean velocities is a subject of active research into sea ice granular rheology (e.g., Herman, 2022) and beyond the scope of the present study.

Still, as shown in Figure 5g, decoupling of the floe-mean ice-ocean velocities due to ice interaction forces varies with both SIC and FSD—and across simulations we obtain empirical fits to $\overline{\langle \|\boldsymbol{\delta_{io}}\|^2 \rangle}$ of the form:

$$\mathbb{D}(r) \equiv \overline{\langle \|\boldsymbol{\delta_{io}}\|^2 \rangle} \propto \exp\left(a_1 c + a_2 r \right), \tag{11}$$

(Figure 7e), for constants a_1 and a_2 that vary as a function of FSD.

The "representative floe size", defined as

$$R \equiv \frac{\int r^3 N(r)\,\mathrm{d}r}{\int r^2 N(r)\,\mathrm{d}r}, \tag{12}$$

was identified as a useful metric of the size distribution of ice floes (Horvat & Tziperman, 2017; Roach et al., 2018; Horvat et al., 2019), and has been used in proposed rheological laws for polydisperse granular media (Herman, 2022). Based on this concept, we employ R to fit the parameters: $a_1 = 0.73R^{0.2}$ and $a_2 = -0.42R^{-1}$ in Equation (11). This method is applicable to the "narrow" power-law-type FSDs examined in this study, but future work will be necessary to gauge the general applicability of this fit to, for example, FSDs spanning a wider floe size range, or other FSD shapes (e.g., log-normal type distributions; Mokus & Montiel, 2022).

3.3.3 Putting it all together

Combining Equation (9) with Equations (10) and (11), we now can estimate $\widetilde{\mathcal{S}}$ using bulk, integrated quantities of the sea ice floe field and the ocean flow field. We write:

$$\frac{\mathcal{S}_{\text{total}}}{\mathcal{A}} = \rho_o C_{io} \int \pi r^2 N(r) \left[\mathbb{P}_o(r) + \mathbb{D}(r)\right]^{3/2} \mathrm{d}r \tag{13}$$

which, for functional forms of $\mathbb{P}_o$ and $\mathbb{D}$, could be evaluated as an expression bulk FSD descriptors ($r_{\min}$, $r_{\max}$ and α). These estimates approximate the scaling and magnitude of the overall model results (dashed lines in Figure 7a), despite a number of simplifying assumptions.

4 Discussion

Here we have provided a simple parameterization of the magnitude and scaling of IOBL turbulence due to ice-ocean interactions across a wide range of floe sizes and sea ice concentrations. The parameterization (Equation (13)) is applicable to a region comparable to a GCM grid cell, and represents the floe-floe and floe-flow interactions that give rise to ocean drag and turbulence. That IOBL turbulence is a scale-dependent sink of ocean kinetic energy that would be unresolved in low resolution continuum models.

The importance of understanding this scale-dependence can be illustrated by comparing $\widetilde{\mathcal{S}}$ to estimates that could be calculated at the GCM grid scale by traditional models. For example, an upper bound can be found by assuming fixed sea ice ($\boldsymbol{u}_i = 0$) at 100% SIC, and using the domain-mean ocean velocity, so $\boldsymbol{u}_{rel} = \widetilde{\boldsymbol{u}}_o$ in Equation (4). This upper limit (Figure 7a, purple line) is nearly two orders-of-magnitude lower than the maximum $\widetilde{\mathcal{S}}$ in our simulations , and significantly less than $\widetilde{\mathcal{S}}$ across the majority of the simulations (except for low SICs with the small FSD case). Thus, floe-scale effects on surface flux can lead to significantly enhanced sub-grid-scale IOBL turbulence that needs to be parameterized to be able to include it in GCMs. This IOBL turbulence is involved in mixing of the upper oceans, deepening of the oceanic boundary layers, entrainment of deeper waters (conceivably including subsurface thermal maxima, e.g., Pham et al., 2023), and the shear within the upper ocean.

Equation (13) reproduces the scaling and magnitude of total IOBL turbulence—depending on just two parameters: the floe size distribution and the ocean kinetic energy spectrum. While several operational-quality GCMs now evolve a prognostic FSD (e.g., Roach et al., 2018, 2019; Boutin et al., 2022), most do not. Thus it may be necessary to perform a simplified concentration-based estimate of the FSD, for example as in Perovich & Jones (2014). Additionally, the sub-grid ocean KE spectrum is not evolved in models. Fox-Kemper & Menemenlis (2008) suggest possible methods to assess and calculate the total sub-grid ocean variance using grid-scale resolved quantities. Following

Reichl & Hallberg (2018), it will be possible to add the extra turbulence production to the oceanic boundary layer vertical mixing scheme.

Using a high-resolution continuum sea ice-ocean coupled model, Shrestha & Manucharyan (2021) showed that the classic Fox-Kemper et al. (2008) parameterization for mixed-layer eddies (MLEs) was suppressed for high sea ice concentrations. They suggest a modification based on turbulent dissipation, ε, parameterized as a function of SIC (shown redimensionalized in Figure 7a as the peach-coloured SM21 line). Indeed, TKE production $\widetilde{\mathcal{S}}$ in most of our simulations exceeds the kinetic energy flux into MLEs ($\rho_o H \frac{\mathrm{d}}{\mathrm{d}t} EKE$ where H is the mixed layer depth) in the ocean model from which the forcing was derived (Figure 7a, pink line) (Lo Piccolo et al., 2023), suggesting that those eddies may be similarly suppressed if we were using a coupled model. To understand these effects, work with future two-way ice-ocean coupled configurations should investigate impacts on spectral shape due to both suppression of MLEs under sea ice (Shrestha & Manucharyan, 2021; Manucharyan & Thompson, 2022), and energization of MLEs due to buoyancy flux at floe edges (Horvat et al., 2016; Gupta & Thompson, 2022), and mixing and momentum vertical transport due to the IOBL turbulence driven by the effects studied here.

There is a marked difference in the SIC dependence of TKE production in our model relative to the dissipation parameterization of Shrestha & Manucharyan (2021) as a result of floe-scale effects. In continuum ice models such as the one used by Shrestha & Manucharyan (2021), ice strength (and associated interaction forces) is negligibly small below SIC ~ 0.8; however, explicit representation of sea ice floes here showed that ice dynamic interactions impact ice-ocean coupling even below this SIC cutoff in a way that depends on the FSD (Section 3.1). Future continuum-model-based approaches for investigating MIZ processes may be appropriate in some contexts, but need to recognize the inherent limitations in not accounting for floe-scale physics.

The parameterization framework developed here can likely be applied in two-way coupled scenarios, with the caveat that energy spectra, $E(k)$ used in Equation (10) will be impacted by the coupling in as-yet unknown ways that will need to be considered. IOBL turbulence will significantly impact the evolution of upper-ocean currents, shear, and boundary layer depth, and we use a one-way coupling in these experiments which does not allow the turbulence produced to have these effects on the ocean. Additionally, the impact of wind was not included in these simulations, and will need to be considered to understand the full range of possible regimes.

Despite some limitations, this study highlights the need to consider scale-dependent effects of sea ice floes on ice-ocean coupling and surface fluxes. We provide a launching point for parameterizing the associated IOBL fluxes of energy based on a floe-scale Reynolds decomposition that separates ice dynamic and ocean dynamic effects on relative velocity. We anticipate that this floe-scale averaging has promise for applicability in all mediated air-sea exchanges, which we propose to continue in future work.

Acknowledgments

All authors on this project are supported through the Scale Aware Sea Ice Project (SASIP). SASIP is supported by Schmidt Futures, a philanthropic initiative that seeks to improve societal outcomes through the development of emerging science and technologies. ALP and BFK have partial support from NSF 2149041. Computing resources were provided by NSF 1655221.

Open Research

All data are available through the Brown Digital Repository (https://repository.library.brown.edu/). Data from the ocean simulation used to force FloeDyn are avail-

able at http://dx.doi.org/10.26300/ak1p-2v10. Output data from the FloeDyn simulations are available at https://repository.library.brown.edu/studio/item/bdr:azg2wtpx/.

References

Armitage, T. W. K., Manucharyan, G. E., Petty, A. A., Kwok, R., & Thompson, A. F. (2020). Enhanced eddy activity in the Beaufort Gyre in response to sea ice loss. *Nature Communications*, *11*(1), 761. doi: 10.1038/s41467-020-14449-z

Bateson, A. W. (2021). *Fragmentation and melting of the seasonal sea ice cover* (Doctoral dissertation, University of Reading). doi: 10.48683/1926.00098821

Boutin, G., Williams, T., Horvat, C., & Brodeau, L. (2022). Modelling the Arctic wave-affected marginal ice zone: A comparison with ICESat-2 observations. *Philosophical Transactions of the Royal Society A: Mathematical, Physical and Engineering Sciences*, *380*(2235), 20210262. doi: 10.1098/rsta.2021.0262

Brenner, S., Rainville, L., Thomson, J., Cole, S., & Lee, C. (2021). Comparing Observations and Parameterizations of Ice-Ocean Drag Through an Annual Cycle Across the Beaufort Sea. *Journal of Geophysical Research: Oceans*, *126*(4). doi: 10.1029/2020JC016977

Brenner, S., Thomson, J., Rainville, L., Crews, L., & Lee, C. (2023). Wind-driven motions of the ocean surface mixed layer in the Western Arctic. *Journal of Physical Oceanography*, *-1*(aop). doi: 10.1175/JPO-D-22-0112.1

Claussen, M. (1990). Area-averaging of surface fluxes in a neutrally stratified, horizontally inhomogeneous atmospheric boundary layer. *Atmospheric Environment. Part A. General Topics*, *24*(6), 1349–1360. doi: 10.1016/0960-1686(90)90041-K

D'Asaro, E. A., Shcherbina, A. Y., Klymak, J. M., Molemaker, J., Novelli, G., Guigand, C. M., ... Özgökmen, T. M. (2018). Ocean convergence and the dispersion of flotsam. *Proceedings of the National Academy of Sciences*, *115*(6), 1162–1167. doi: 10.1073/pnas.1718453115

Delpech, A., Barkan, R., Renault, L., McWilliams, J., Siyanbola, O. Q., Buijsman, M. C., & Arbic, B. K. (2023). Wind-current feedback is an energy sink for oceanic internal waves. *Sci Rep*, *13*(1), 5915. doi: 10.1038/s41598-023-32909-6

Eayrs, C., Li, X., Raphael, M. N., & Holland, D. M. (2021). Rapid decline in Antarctic sea ice in recent years hints at future change. *Nature Geoscience*, *14*(7), 460–464. doi: 10.1038/s41561-021-00768-3

Feltham, D. L. (2008). Sea Ice Rheology. *Annu. Rev. Fluid Mech.*, *40*(1), 91–112. doi: 10.1146/annurev.fluid.40.111406.102151

Fox-Kemper, B., Danabasoglu, G., Ferrari, R., Griffies, S. M., Hallberg, R. W., Holland, M. M., ... Samuels, B. L. (2011). Parameterization of mixed layer eddies. III: Implementation and impact in global ocean climate simulations. *Ocean Modelling*, *39*(1), 61–78. doi: 10.1016/j.ocemod.2010.09.002

Fox-Kemper, B., Ferrari, R., & Hallberg, R. (2008). Parameterization of mixed layer eddies. Part I: Theory and diagnosis. *J. Phys. Oceanogr.*, *38*(6), 1145–1165. doi: 10.1175/2007JPO3792.1

Fox-Kemper, B., & Menemenlis, D. (2008). Can Large Eddy Simulation Techniques Improve Mesoscale-Rich Ocean Models? In M. Hecht & H. Hasumi (Eds.), *Ocean Modeling in an Eddying Regime* (Vol. 177, pp. 319–338). AGU Geophysical Monograph Series.

Golden, K. M., Bennetts, L. G., Cherkaev, E., Eisenman, I., Feltham, D., Horvat, C., ... Wells, A. J. (2020). Modeling Sea Ice. *Notices of the American Mathematical Society*, *67*(10), 1. doi: 10.1090/noti2171

Gupta, M., & Thompson, A. F. (2022). Regimes of sea-ice floe melt: Ice-ocean coupling at the submesoscales. *Journal of Geophysical Research: Oceans*, *n/a*(n/a), e2022JC018894. doi: 10.1029/2022JC018894

Herman, A. (2013). Numerical modeling of force and contact networks in fragmented sea ice. *Annals of Glaciology*, *54*(62), 114–120. doi: 10.3189/2013AoG62A055

Herman, A. (2022). Granular effects in sea ice rheology in the marginal ice zone. *Phil Trans R Soc A*(MIZ).

Horvat, C., Roach, L. A., Tilling, R., Bitz, C. M., Fox-Kemper, B., Guider, C., ... Shepherd, A. (2019). Estimating the sea ice floe size distribution using satellite altimetry: Theory, climatology, and model comparison. *The Cryosphere*, *13*(11), 2869–2885. doi: 10.5194/tc-13-2869-2019

Horvat, C., & Tziperman, E. (2017). The evolution of scaling laws in the sea ice floe size distribution. *Journal of Geophysical Research: Oceans*, *122*(9), 7630–7650. doi: 10.1002/2016JC012573

Horvat, C., Tziperman, E., & Campin, J.-M. (2016). Interaction of sea ice floe size, ocean eddies, and sea ice melting. *Geophys. Res. Lett.*, *43*(15), 8083–8090. doi: 10.1002/2016GL069742

Lopez-Acosta, R., Schodlok, M. P., & Wilhelmus, M. M. (2019). Ice Floe Tracker: An algorithm to automatically retrieve Lagrangian trajectories via feature matching from moderate-resolution visual imagery. *Remote Sensing of Environment*, *234*(October), 111406. doi: 10.1016/j.rse.2019.111406

Lo Piccolo, A. (2021). *Arctic ocean submesoscale brine driven eddies: modeling of a sea ice edge front* (Tesi di laurea). University of Bologna.

Lo Piccolo, A., Horvat, C., & Fox-Kemper, B. (2023). *Energetics and transfer of submesoscale brine driven eddies at a sea ice edge* [Paper Submitted for Publication].

Lüpkes, C., Gryanik, V. M., Hartmann, J., & Andreas, E. L. (2012). A parametrization, based on sea ice morphology, of the neutral atmospheric drag coefficients for weather prediction and climate models. *Journal of Geophysical Research Atmospheres*, *117*(13), D13112. doi: 10.1029/2012JD017630

Manucharyan, G. E., Lopez-Acosta, R., & Wilhelmus, M. M. (2022). Spinning ice floes reveal intensification of mesoscale eddies in the western Arctic Ocean. *Sci Rep*, *12*(1), 7070. doi: 10.1038/s41598-022-10712-z

Manucharyan, G. E., & Thompson, A. F. (2022). Heavy footprints of upper-ocean eddies on weakened Arctic sea ice in marginal ice zones. *Nature Communications*, *13*(1), 2147. doi: 10.1038/s41467-022-29663-0

Marshall, J., Adcroft, A., Hill, C., Perelman, L., & Heisey, C. (1997). Hydrostatic, quasi-hydrostatic and nonhydrostatic ocean modeling. *J. Geophys. Res.*, *102, C3*, 5733–5752.

Martin, T., Steele, M., & Zhang, J. (2014). Seasonality and long-term trend of Arctic Ocean surface stress in a model. *J. Geophys. Res. Oceans*, *119*(3), 1723–1738. doi: 10.1002/2013JC009425

McPhee, M. G. (1980). An analysis of pack ice drift in summer. *Sea ice processes and models*, 62–75.

Meier, W., & Stroeve, J. (2022). An Updated Assessment of the Changing Arctic Sea Ice Cover. *Oceanog.* doi: 10.5670/oceanog.2022.114

Meneghello, G., Doddridge, E., Marshall, J., Scott, J., & Campin, J.-M. (2020). Exploring the Role of the "Ice–Ocean Governor" and Mesoscale Eddies in the Equilibration of the Beaufort Gyre: Lessons from Observations. *Journal of Physical Oceanography*, *50*(1), 269–277. doi: 10.1175/JPO-D-18-0223.1

Mokus, N. G. A., & Montiel, F. (2022). Wave-triggered breakup in the marginal ice zone generates lognormal floe size distributions: A simulation study. *The Cryosphere*, *16*(10), 4447–4472. doi: 10.5194/tc-16-4447-2022

Ou, H. W., & Gordon, A. L. (1986). Spin-down of baroclinic eddies under sea ice. *Journal of Geophysical Research: Oceans*, *91*(C6), 7623–7630. doi: 10.1029/JC091iC06p07623

Perovich, D. K., & Jones, K. F. (2014). The seasonal evolution of sea ice floe size distribution. *J. Geophys. Res. Oceans*, *119*(12), 8767–8777. doi: 10.1002/

2014JC010136

Pham, H. T., Sarkar, S., Johnson, L., Fox-Kemper, B., Sullivan, P. P., & Li, Q. (2023). Multi-Scale Temporal Variability of Turbulent Mixing During a Monsoon Intra-Seasonal Oscillation in the Bay of Bengal: An LES Study. *Journal of Geophysical Research: Oceans*, *128*(1), e2022JC018959. doi: 10.1029/2022JC018959

Rabatel, M. (2015). *Modélisation dynamique d'un assemblage de floes rigides* (Unpublished doctoral dissertation). Université Grenoble Alpes.

Rabatel, M., Labbé, S., & Weiss, J. (2015). Dynamics of an assembly of rigid ice floes. *Journal of Geophysical Research: Oceans*, *120*(9), 5887–5909. doi: 10.1002/2015JC010909

Rainville, L., Lee, C., & Woodgate, R. A. (2011). Impact of wind-driven mixing in the Arctic Ocean. *Oceanography*, *24*(3), 136–145.

Reichl, B. G., & Hallberg, R. (2018). A simplified energetics based planetary boundary layer (ePBL) approach for ocean climate simulations. *Ocean Modelling*, *132*, 112–129. doi: 10.1016/j.ocemod.2018.10.004

Renault, L., Molemaker, M. J., McWilliams, J. C., Shchepetkin, A. F., Lemarié, F., Chelton, D., ... Hall, A. (2016). Modulation of Wind Work by Oceanic Current Interaction with the Atmosphere. *Journal of Physical Oceanography*, *46*(6), 1685–1704. doi: 10.1175/JPO-D-15-0232.1

Roach, L. A., Bitz, C. M., Horvat, C., & Dean, S. M. (2019). Advances in Modeling Interactions Between Sea Ice and Ocean Surface Waves. *Journal of Advances in Modeling Earth Systems*, *11*(12), 4167–4181. doi: 10.1029/2019MS001836

Roach, L. A., Horvat, C., Dean, S. M., & Bitz, C. M. (2018). An emergent sea ice floe size distribution in a global coupled ocean–sea ice model. *Journal of Geophysical Research: Oceans*, *123*(6), 4322–4337. doi: 10.1029/2017JC013692

Rolph, R. J., Feltham, D. L., & Schröder, D. (2020). Changes of the Arctic marginal ice zone during the satellite era. *The Cryosphere*, *14*(6), 1971–1984. doi: 10.5194/tc-14-1971-2020

Rynders, S., Aksenov, Y., Feltham, D. L., Nurser, A. J. G., & Madec, G. (2022). Impact of Granular Behaviour of Fragmented Sea Ice on Marginal Ice Zone Dynamics. In J. Tuhkuri & A. Polojärvi (Eds.), *IUTAM Symposium on Physics and Mechanics of Sea Ice* (pp. 261–274). Cham: Springer International Publishing. doi: 10.1007/978-3-030-80439-8_13

Shen, H. H., Hibler, W. D., Lepparanta, M., & Leppäranta, M. (1987). The role of floe collisions in sea ice rheology. *Journal of Geophysical Research*, *92*(C7), 7085–7096. doi: 10.1029/JC092iC07p07085

Shrestha, K., & Manucharyan, G. E. (2021). Parameterization of submesoscale mixed layer restratification under sea ice. *Journal of Physical Oceanography*, *-1*(aop). doi: 10.1175/JPO-D-21-0024.1

Smith, M., & Thomson, J. (2019). Ocean Surface Turbulence in Newly Formed Marginal Ice Zones. *Journal of Geophysical Research: Oceans*, *124*(3), 1382–1398. doi: 10.1029/2018JC014405

Stern, H. L., Schweiger, A. J., Zhang, J., & Steele, M. (2018). On reconciling disparate studies of the sea-ice floe size distribution. *Elem. Sci. Anth.*, *6*(1), 49. doi: 10.1525/elementa.304

Strong, C., & Rigor, I. G. (2013). Arctic marginal ice zone trending wider in summer and narrower in winter. *Geophysical Research Letters*, *40*(18), 4864–4868. doi: 10.1002/grl.50928

Timmermans, M.-L., Cole, S., & Toole, J. (2012). Horizontal Density Structure and Restratification of the Arctic Ocean Surface Layer. *J. Phys. Oceanogr.*, *42*(4), 659–668. doi: 10.1175/JPO-D-11-0125.1

Timmermans, M.-L., & Marshall, J. (2020). Understanding Arctic Ocean Circulation: A Review of Ocean Dynamics in a Changing Climate. *Journal of Geophysical Research: Oceans*, *125*(4), e2018JC014378. doi: 10.1029/2018JC014378

Tsamados, M., Feltham, D. L., Schroeder, D., Flocco, D., Farrell, S. L., Kurtz, N., ... Bacon, S. (2014). Impact of variable atmospheric and oceanic form drag on simulations of Arctic sea ice. *J. Phys. Oceanogr.*, *44*(5), 1329–1353. doi: 10.1175/JPO-D-13-0215.1

Wang, Q., Marshall, J., Scott, J., Meneghello, G., Danilov, S., & Jung, T. (2019). On the Feedback of Ice–Ocean Stress Coupling from Geostrophic Currents in an Anticyclonic Wind Regime over the Beaufort Gyre. *Journal of Physical Oceanography*, *49*(2), 369–383. doi: 10.1175/JPO-D-18-0185.1

Wenta, M., & Herman, A. (2018). The influence of the spatial distribution of leads and ice floes on the atmospheric boundary layer over fragmented sea ice. *Ann. Glaciol.*, *59*(76pt2), 213–230. doi: 10.1017/aog.2018.15

Wenta, M., & Herman, A. (2019). Area-Averaged Surface Moisture Flux over Fragmented Sea Ice: Floe Size Distribution Effects and the Associated Convection Structure within the Atmospheric Boundary Layer. *Atmosphere*, *10*(11), 654. doi: 10.3390/atmos10110654

Wu, Y., Wang, Z., & Liu, C. (2021). Impacts of Changed Ice-Ocean Stress on the North Atlantic Ocean: Role of Ocean Surface Currents. *Front. Mar. Sci.*, *8*, 628892. doi: 10.3389/fmars.2021.628892

Figure 1.

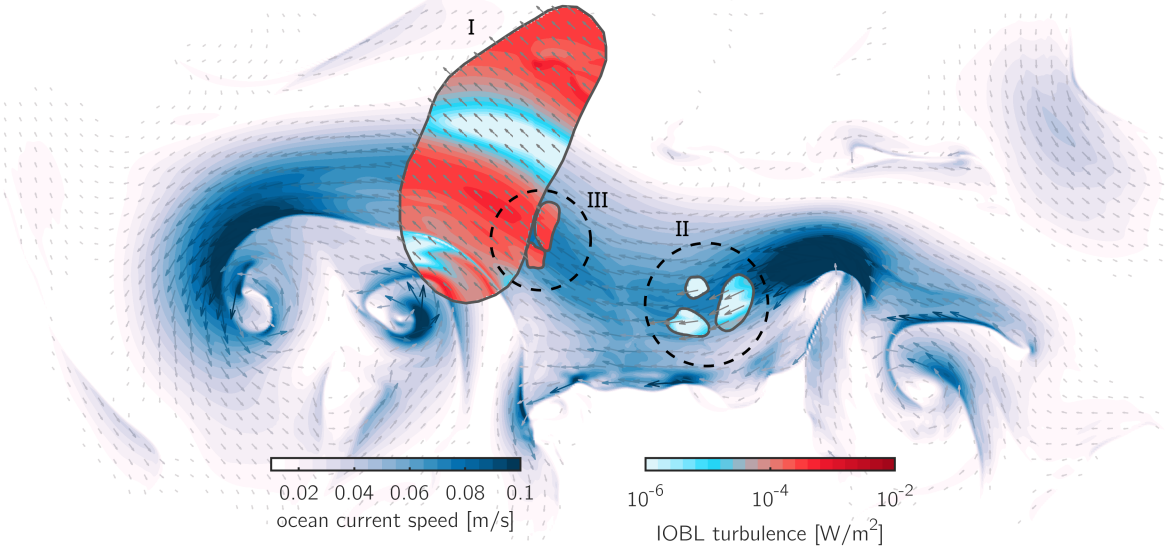
I
II
III
0.02 0.04 0.06 0.08 0.1
ocean current speed [m/s]
10^{-6} 10^{-4} 10^{-2}
IOBL turbulence [W/m^2]

Figure 2.

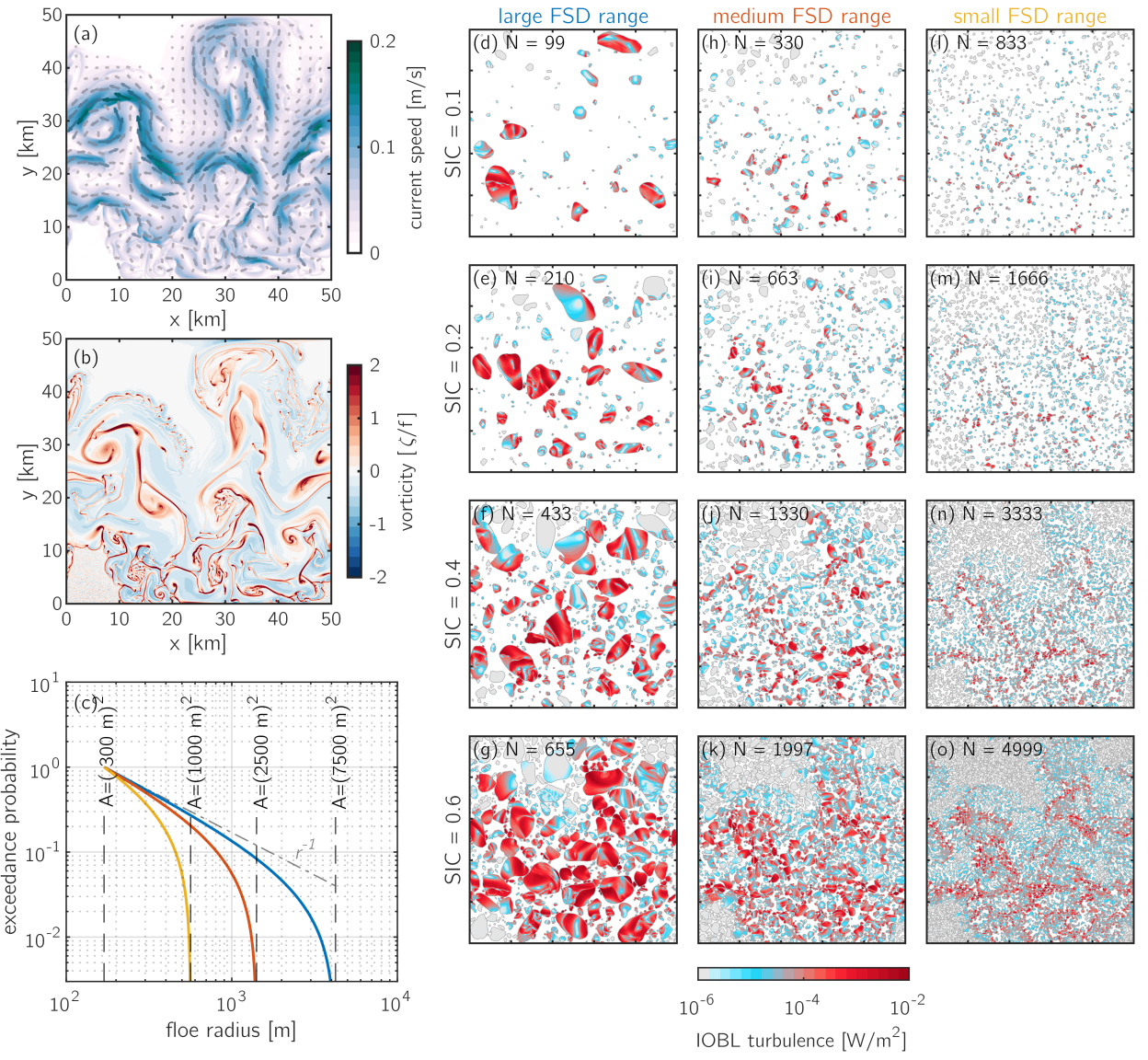
large FSD range
medium FSD range
small FSD range
SIC = 0.1
SIC = 0.2
SIC = 0.4
SIC = 0.6
(a)
(b)
(c)
(d) N = 99
(e) N = 210
(f) N = 433
(g) N = 655
(h) N = 330
(i) N = 663
(j) N = 1330
(k) N = 1997
(l) N = 833
(m) N = 1666
(n) N = 3333
(o) N = 4999
y [km]
x [km]
current speed [m/s]
vorticity [ζ/f]
exceedance probability
floe radius [m]
A=(300 m)²
A=(1000 m)²
A=(2500 m)²
A=(7500 m)²
r⁻¹
IOBL turbulence [W/m²]

FIgure 3.

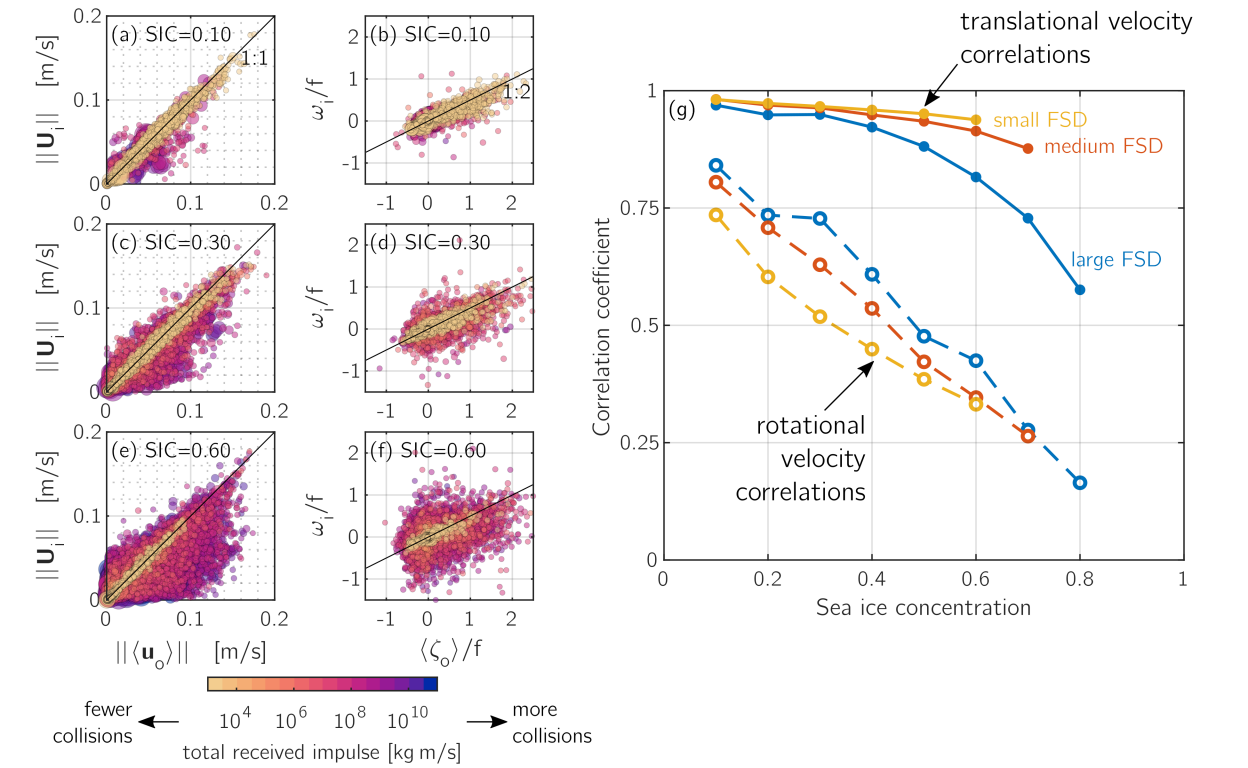
(a) SIC=0.10
1:1
(b) SIC=0.10
1:2
(c) SIC=0.30
(d) SIC=0.30
(e) SIC=0.60
(f) SIC=0.60
$||\mathbf{U}_i||$ [m/s]
ω_i/f
$||\langle \mathbf{u}_o \rangle||$ [m/s]
$\langle \zeta_o \rangle/f$
fewer collisions
more collisions
10^4 10^6 10^8 10^{10}
total received impulse [kg m/s]
translational velocity correlations
(g)
small FSD
medium FSD
large FSD
rotational velocity correlations
Correlation coefficient
Sea ice concentration

Figure 4.

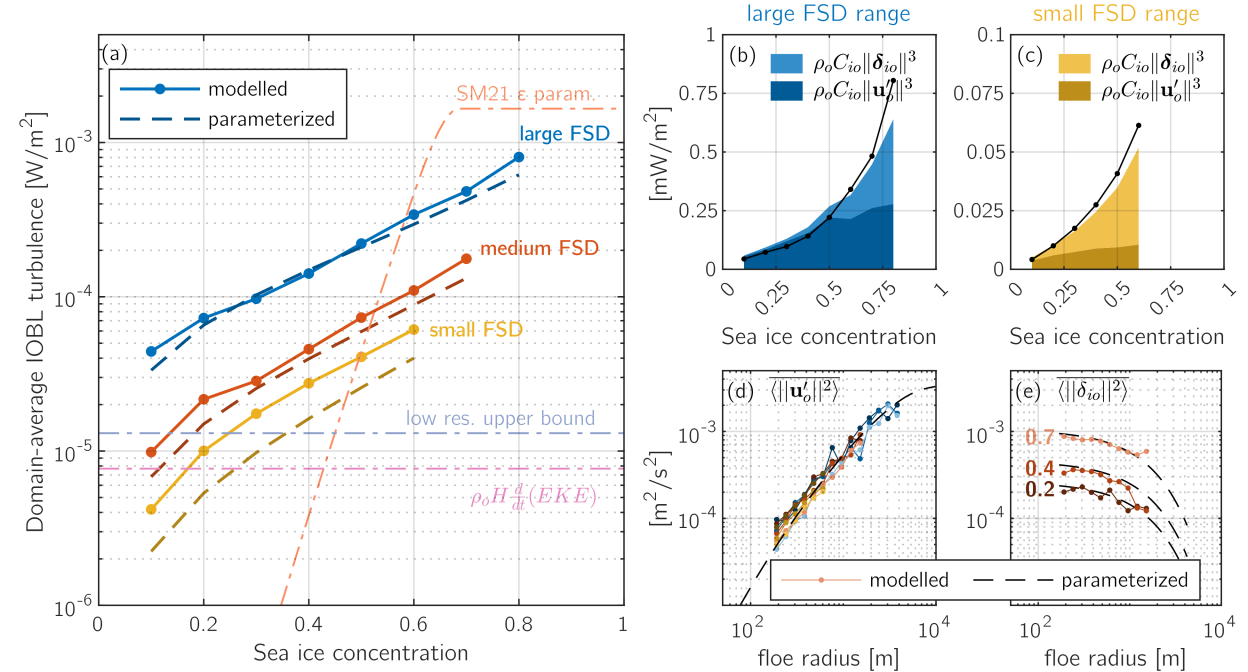
(a)
modelled
parameterized
SM21 ε param.
large FSD
medium FSD
small FSD
low res. upper bound
$\rho_o H \frac{d}{dt}\langle EKE \rangle$
Domain-average IOBL turbulence [W/m^2]
Sea ice concentration
large FSD range
small FSD range
(b)
(c)
$\rho_o C_{io} \|\boldsymbol{\delta}_{io}\|^3$
$\rho_o C_{io} \|\mathbf{u}'_o\|^3$
[mW/m^2]
Sea ice concentration
(d)
$\overline{\langle ||\mathbf{u}'_o||^2 \rangle}$
(e)
$\overline{\langle ||\delta_{io}||^2 \rangle}$
0.7
0.4
0.2
[m^2/s^2]
modelled
parameterized
floe radius [m]
floe radius [m]